FULL PAPER

Subpicosecond Domain Switching in Discrete Regions of $Pb(Zr_{0.35}Ti_{0.65})O_3$ Thick Films

An Quan Jiang, Zhi Hui Chen, Wen Yuan Hui, Dongping Wu, and James F. Scott**

The time dependence of the domain switching current density, $J_{sw}(t)$, under pulsed voltages on a ferroelectric parallel-plate capacitor is the consequence of region-by-region polarization reversals across the film. As the distributive coercive voltage of domain nucleation increases from zero to the maximum applied voltage during the capacitor charging time, $J_{sw}(t)$ is proportional to the domain switching speed at each time. By transforming the spatially inhomogeneous domain nucleation distribution into a temporal distribution of coercive fields (E_c), a local $\ln J_{sw}$ versus E_c^{-1} plot is derived for each domain, following the Merz equation. This provides insight into the independent domain switching dynamics at different nucleation sites in $Pb(Zr_{0.35}Ti_{0.65})O_3$ thick films over a large current range. Although the activation field of the slope of the $\ln J_{sw}(t)$ versus E_c^{-1} plot varies with film area and temperature, all the plots extrapolate to a single point (J_0, E_0) from which the ultimate domain switching current density of $J_0 = 1.4 \times 10^8$ A cm^{-2} at the highest field of E_0 = 0.20-0.25 MV cm^{-1} is derived. Unexpectedly, J_0 and E_0 are independent of the film thickness and area, after correction for a small interfacial-layer effect. This analysis provides rigorous evidence for nucleation rate-limited domain switching with a subpicosecond nucleation time and the relative unimportance of domain forward-growth time across film thicknesses between 0.14 and 2 μm. This work paves the way to improve the efficiency of ferroelectric thick-film functionality in electronic and optoelectronic devices with ultrafast clock rates.

1. Introduction

Ferroelectric materials that are both piezoelectric and pyroelectric exhibit reversible spontaneous polarization, which is applicable in several fields, including electronics, photonics, sensors, catalysts, energy harvesting, and information storage, with high performance in memories, actuators, vibration sensors, and other devices. The ultrafast polarization switching dynamics in both thin and thick films play an important role in terms of the device operating speeds.[1–6] This ultrafast functionality is field dependent and approaches picosecond speeds, as demonstrated in the non-destructive retrieval of terahertz emission data caused by depolarization under laser illumination.[7] In contrast, the fastest time reported from direct experimental observation using electrical pulses on parallel-plate ferroelectric capacitors is as long as 220 ps because of instrumental limitations.[8] From the coercive field (E_c) dependence of the domain switching current density (J_{sw}) spanning more than five orders of magnitude in a 140-nm-thick $Pb(Zr_{0.4}Ti_{0.6})O_3$ thin film via an improved pulse-type characterization technique, a subpicosecond domain switching process was asymptotically predicted from a modified Merz Equation (1) when $J_{sw} \propto v$: [9]

$$J_{sw} = J_0 \exp\left[-\alpha\left(\frac{1}{E_c} - \frac{1}{E_0}\right)\right] \quad (1)$$

where v is a switching speed incorporating both domain nucleation and growth, α is the activation field, and J_0 is the ultimate domain switching current density at a saturation field of E_0. Generally in reported experiments the domain switching time is current-limited by two things: 1) the total resistance, R_t, including the internal resistance of the pulse generator, i.e., $R_t \neq 0$, and 2) the ability of the voltage source to deliver the necessary current in a very short time.[17] Consequently, the lower bound of the sub-picosecond time of ≈0.47 ps is calculated from the equation $\tau_0 = 2P_s/J_0$, which coincides with the value of $\tau_0 \approx 10^{-13}$ s implied by the E(TO) soft-mode frequency in $Pb(Zr_{0.4}Ti_{0.6})O_3$ assuming phonon relaxation mechanisms;[10,11] here P_s is the saturation polarization. All the $\ln J_{sw}$ vs. E^{-1} plots at different temperatures (T) cross at the point (J_0, E_0) with $J_0 = 1.4 \times 10^8$ A cm^{-2} and $E_0 = 0.20$ MV cm^{-1}.

It is useful to compare the present technique with the beautiful atomic force microscopy studies: piezo-force techniques by Kalinin's group showed the ability to measure switching parameters near specific defects.[12] In general, we find the two techniques complementary. Theoretically, polarization reversal occurs via the nucleation of an oppositely polarized domain at a preferred site with lattice imperfections, such as defects (oxygen vacancies), dislocations, inclusions, grain boundaries, rough walls of the opposite domains, and edges

Prof. A. Q. Jiang, Z. H. Chen, W. Y. Hui, Prof. D. P. Wu
State Key Laboratory of ASIC & System
Department of Microelectronics
Fudan University
Shanghai, 200433, China
E-mail: aqjiang@fudan.edu.cn
Prof. J. F. Scott
Department of Physics
University of Cambridge
Cambridge CB3 0HE, UK
E-mail: jfs32@hermes.cam.ac.uk

DOI: 10.1002/adfm.201102829

of ferroelectric nanostructures,[2,12–15] followed by forward growth from an initially spherical embryonic nanodomain. According to classical domain nucleation models,[12,13,16–23] the domain nucleation probability is high near these preferred sites with lowered nucleation energy barriers, and the polarization reversal is nucleation-rate limited ignoring the wall forward-growth time. If this theory is correct, the asymptotic value of τ_0 is the ultimate domain nucleation time, which is film-thickness independent. But this hypothesis is still unchecked in experiments. In this sense, the relevant evidence is required to support this nucleation model after exclusion of the film thickness effect.

Experimental observations of the moving domain walls from piezoresponse force microscopy (PFM) with a focused field near the local defect sites indentified a defect-controlled nucleation mechanism with a spatial nucleation energy distribution,[12] apart from the consequent field dependence of the wall sideways motion.[24,25] These nucleation sites can be determined repeatedly via coercive-field imaging across the film area.[12,25] However, the PFM characterization speed over small regions is insufficiently fast to detect rapid polarization change, although 100 ns can be achieved using a pump-probe technique.[26] Moreover, this type of technique, with an inhomogeneous switching field, neglects domains that do not fully penetrate the film thickness. In comparison, the space- and field-averaged domain switching speed of pulse measurements on a parallel-plate capacitor under a uniform switching field can cover several orders of magnitude and is more suitable for the study of an ultrafast domain switching response.[27] Unfortunately, this method has limited application to films with a narrow E_c distribution.[9] Difficulties would arise in films that consist of multiple regions with a broad distribution of domain nucleation energies.

The polarization reversal generally occurs first at regions with a small coercive voltage (V_c), as the applied voltage (V) across the film gradually increases from 0 to V during the capacitor charging time (t). The switching current for these regions is:[28]

$$I_{sw} = (V - V_c)/R_t \quad (2)$$

After completion of the polarization reversal in these regions, the domains in other regions with a higher V_c value begin to switch in sequence. Therefore, the domain switching current under application of the pulse is an ensemble of many current steps because of the spatial V_c distribution across the defect-mediated nucleation sites. In other words, this current transient is the real-space transformation of the domain switching currents in regions with different thermal energies into a time order, with coercive voltages of $0 < V_c(t_1) < V_c(t_2) < V_c(t_3) < \ldots \leq V$ and currents of $V/R_t > I_{sw}(t_1) > I_{sw}(t_2) > I_{sw}(t_3) > \ldots \geq 0$, where $0 < t_1 < t_2 < t_3 < \ldots$. These independent switching regions have been repeatedly observed experimentally by PFM imaging of the local polarization reversals with a step-by-step increase in the applied voltage.[13] With time discretization of the current transient into many regions, it is possible to delve into the profound and complex domain nucleation of each region over a large switching current range, and thus, t_0 and E_0 can be independently derived from these regions for comparison of the local defect-mediated nucleation mechanisms.

2. Results and Discussion

To understand the film thickness effect on the ultimate domain switching time, $Pb(Zr_{0.35}Ti_{0.65})O_3$ (PZT) films thicknesses of 0.15–2 μm were prepared by sol-gel spin-coating on $Pt/TiO_2/SiO_2/Si$ substrates. All of the films are perovskite in structure with a major (111) orientation of the columnar grains, as observed from X-ray diffraction patterns and scanning electron microscopy (Supporting Information Figure S1a–c and Figure S2a–f).

Figure 1a,b shows both the temperature and film thickness dependences of the polarization–electric (*P–E*) hysteresis loops. Although the loops are nearly square, two kinks appear in the vicinity of the positive and negative coercive fields ($E_c^{+/-}$), suggesting of the coexistence at the two regions (a) and (b) of smaller and larger coercive fields in the films. Because the loops are asymmetric, we define $E_c = (E_c^+ - E_c^-)/2$ to accurately describe the mean coercive field. These two regions may originate from film inhomogeneities such as composition fluctuations and/or 180°/90° walls.[2] The resulting domain switching

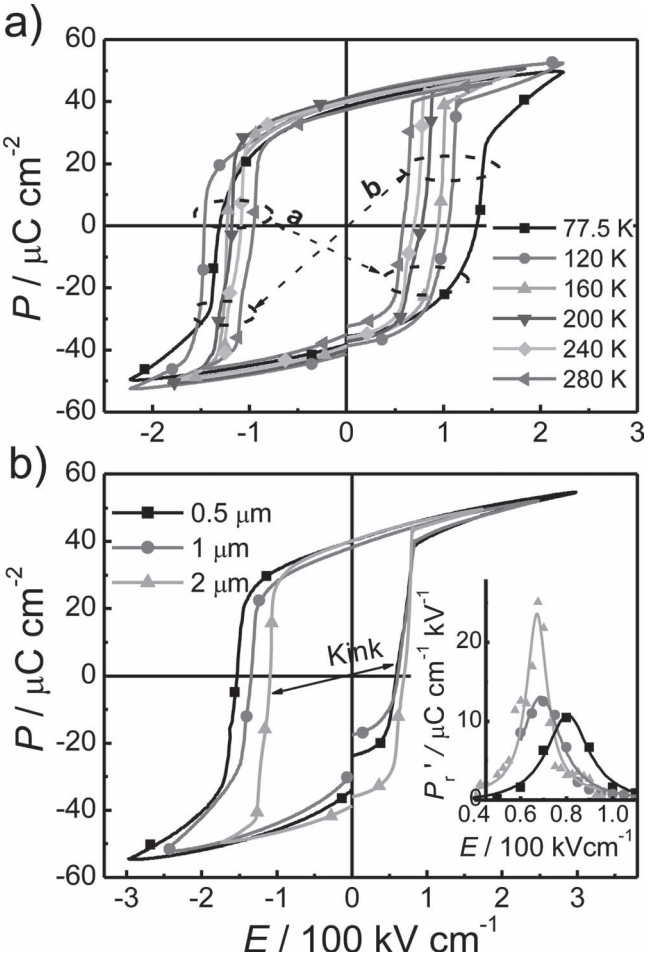

Figure 1. a) *P–E* hysteresis loops at 1 kHz for PZT with thickness of 2 μm at different temperatures. b) *P–E* hysteresis loops at 1 kHz for PZT with different thicknesses at 240 K. The inset shows the coercive-field distribution of the films and the dependence of the differential remanent polarization on the field.

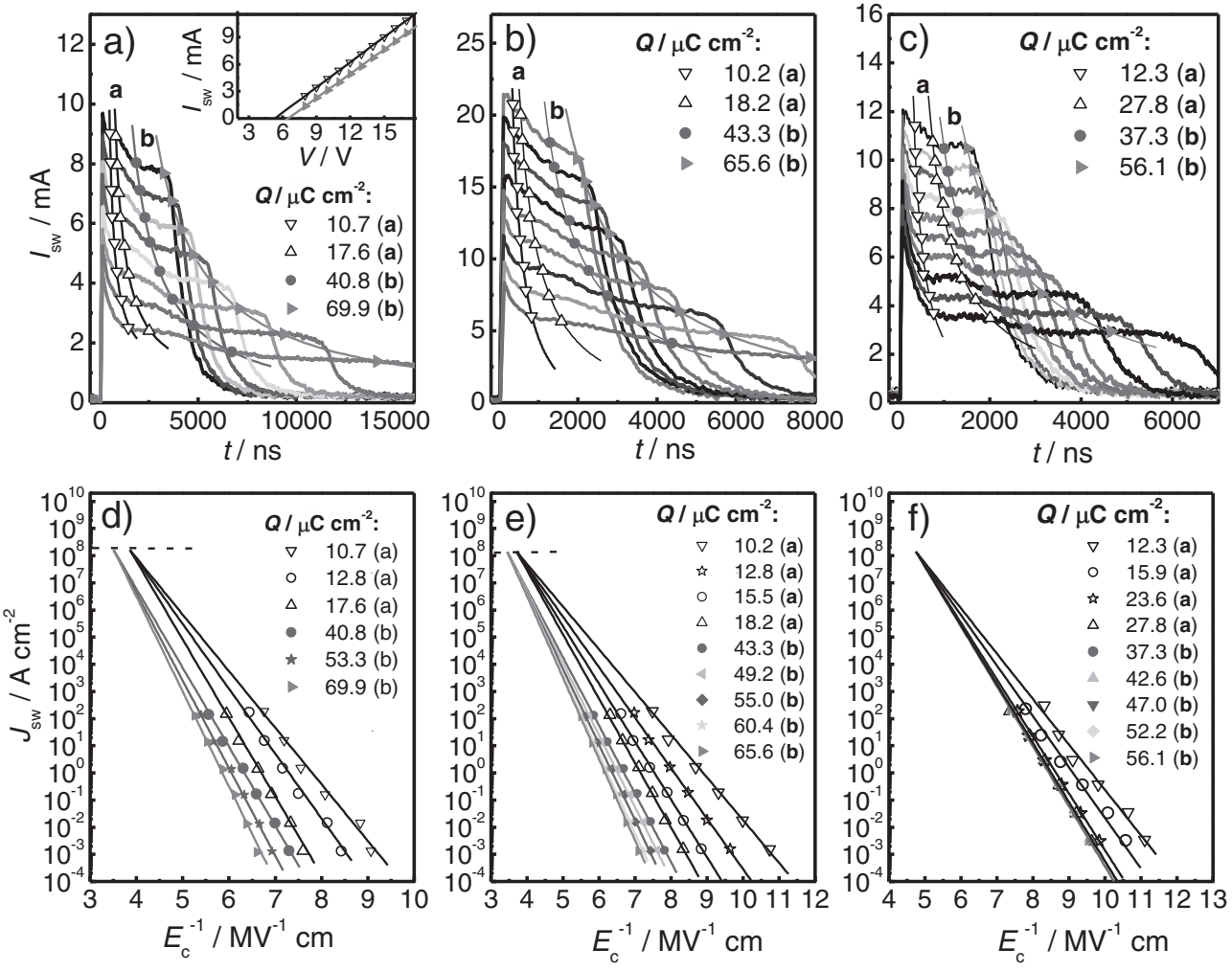

Figure 2. Domain switching current transients across R_t = 1 kΩ for PZT with thicknesses of: a) 0.5 μm at 77.5 K under increasing voltage of V = 8–15 V in steps of 1 V; b) 1 μm at 77.5 K under V = 16–32 V in steps of 2 V; and c) 2 μm at 120 K under V = 26–35 V in steps of 1 V. Each curve shows two typical current plateaus at inhomogeneous regions (a) and (b). The current position to vary with V for an independent domain with a coercive voltage of V_c is pinned from the charge integration equal to Q, as shown by the symbols, where the solid lines are the visual guides. V_c for the domain is derived from the intercept of a linear I_{sw}–V plot with the V axis, as shown by the inset in a). Panels (d–f) show corresponding semilogarithmic J_{sw}–E^{-1} dependences of the above individual domains with different nucleation energies across the film area.

currents of the films with thicknesses of 0.5 μm, 1 μm, and 2 μm, denoted as PZT1, PZT2 and PZT3, respectively, were measured using in-series resistors with total resistance of R_t under square pulses with voltages of $V(t)$, as shown in **Figure 2**a–c. Before each switching pulse, all of the domains were preset with the polarity opposite to that of the applied voltage. The voltage transient $V_R(t)$ across R_t is measured by an oscilloscope, and the switching current is:

$$I_{sw}(t) = V_R(t) / R_t \quad (3)$$

The domain switching current transient is generally a flat plateau if the V_c distribution is narrow enough.[9,28] From the current plateau height, it is possible to derive J_{sw} and E_c, which are largely adjustable via the input R_t spanning from 100 Ω to 100 MΩ; once I_{sw} is fixed, J_{sw} can be reversely adjusted via electrode area scaled from 10^{-6} to 2.5×10^{-3} cm^2 in ref. [9], where the electrode size is far larger than the distance (approximately submicrometer)[12]) between nucleation sites of domains. From our experiments, the two J_{sw}–E_c^{-1} plots always merge together. Therefore, we adopt the former method as one of choices to adjust J_{sw} for the convenience of our characterization. From the modified Merz Equation (1), the asymptotic J_0 and E_0 values are extrapolated from the intersection of all $\ln J_{sw}$–$1/E_c$ plots at the point (J_0,E_0) at different temperatures.[9] However, most films have an E_c distribution, as implied by the dP_r/dE versus E plots in the inset of Figure 1b, where P_r is the remanent polarization, i.e., half of the difference between domain switching and nonswitching polarizations under two negative-positive and positive-positive pulse sequences.[28] The peak reflects the E_c^+ distribution, which is broad in PZT1 but narrow in PZT3, and the peak position corresponds to the average coercive field in the P–E hysteresis loop. This E_c^+ distribution describes the

diversity of the local nucleation energy barriers, ΔU, with $v \propto \exp(-\Delta U/k_B T)$. This means that from region to region across the film area, the domain switching speed varies considerably under the same applied voltage because of the local defect-mediated nucleation barriers. Therefore, $I_{sw}(t)$ under V is the current consequence of these regions ordered as $0 < t_1 < t_2 < t_3 < \ldots$ with $0 < V_c(t_1) < V_c(t_2) < V_c(t_3) < \ldots$ and $V/R_t > I_{sw}(t_1) > I_{sw}(t_2) > I_{sw}(t_3) > \ldots$. For example, each current plateau in Figure 2a–c consists of the two major steps of inhomogeneous regions **a** and **b** with $V_c^{(a)} < V_c^{(b)}$ and $I_{sw}(a) > I_{sw}^{(b)}$, in agreement with the twisted P–E hysteresis loops shown in Figure 1a,b (domain nucleation within each region is also inhomogeneous). Separation of the J_{sw}–E_c dependence from the current transient for an independent domain localized at a specific region is a key factor in the understanding of the local domain switching dynamics.

During the capacitor charging time, the voltage across the ferroelectric capacitor, C_f, increases gradually from $0 \rightarrow V_c(t_1) \rightarrow V_c(t_2) \rightarrow V_c(t_3) \ldots \rightarrow V$. After the completion of the previous domain switching, the next domain with a higher coercive voltage begins to reverse, and the total charge density, $Q(t) = \int_0^t \frac{I_{sw}(t)}{S} dt$, at this moment is:

$$Q(t) = \int_0^{V_c^m} \frac{C_f(V)}{S} dV + \sum_{i=1}^{m} \Delta P^i \left(V_c^i\right) \quad (4)$$

where S is the electrode area. The first term on the right is the nonlinear capacitor charging and the second is the sum of all polarizations ΔP^i across the regions until the domain at the m^{th} region begins to reverse. This charge remains nearly constant for current transients under different values of V, as shown by the open and closed symbols within the regions (a) and (b) in Figure 2a–c. From these positions we can separate the I_{sw}–V plot for each domain, as shown in the inset of Figure 2a. From the extension of the linear plot to the V axis, we can accurately determine $V_c^{(m)}$ from Equation (2) and thus, determine the final J_{sw}–E_c^{-1} plots for each domain, as shown in Figure 2d–f for PZT1, PZT2, and PZT3, respectively. The linear extrapolation can effectively eliminate the other resistive effects of non-ferroelectric layers on $V_c^{(m)}$, e.g., the interfacial conductive electrode-layer extension into the film thickness.[9]

All of the plots from the different domains with various nucleation energies across the film area follow the modified Merz Equation (1), as shown from the solid-line fitting of the data in Figure 2d–f, and the plots cross exactly at the point (J_0, E_0). It seems that the ultimate domain switching current of $J_0 = 1.4 \times 10^8$ A cm^{-2} is constant across the film area and film thickness from 0.14 to 2 μm, regardless of the diverging domain nucleation energies. However, E_0 differs by 9.1%, 6.9%, and nearly 0% between regions (a) and (b) for PZT1, PZT2, and PZT3, respectively, because of the film inhomogeneity, but it remains constant within either region. Additionally, the slope (α) of the $\ln J_{sw}$–$1/E_c$ plot shows a greater dispersion over the film area in region (a) than in region (b). Finally, this dispersion disappears from region (b) with increasing film thickness up to 2 μm in Figure 2f, in agreement with the sharpened dP_r/dE peak in PZT3 in the inset of Figure 1b. This α dispersion within either region (a) or (b) reflects the importance of the defect-mediated domain nucleation energies on E_c at low J_{sw} values rather than E_0 at J_0.

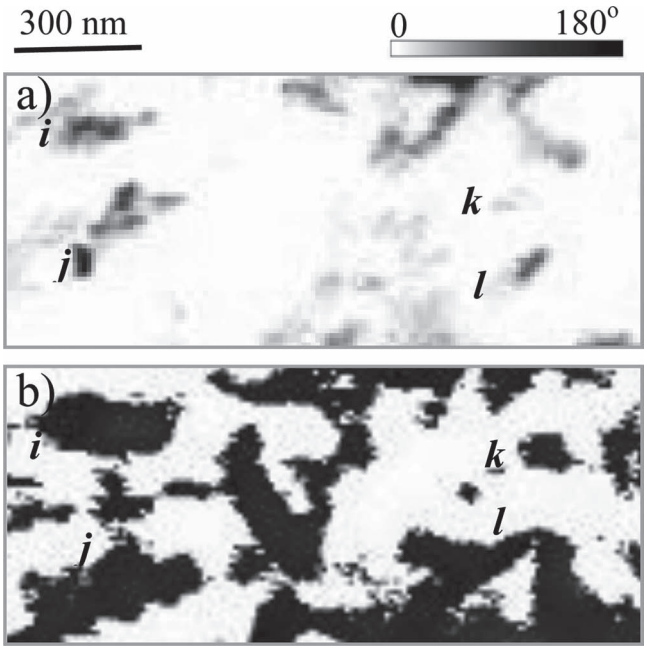

Figure 3. PFM phase images of the 300 nm-thick $Pb(Zr_{0.35}Ti_{0.65})O_3$ film at two poling voltages of a) +10 V and b) –4 V. The domain switching at –4 V starts in the vicinity of imperfections, such as opposite domains *i*, *j*, *k*, and *l*.

PFM phase imaging of the 300 nm-thick PZT poled at –10 V shows the presence of imperfections in the opposite domains at positions such as *i*, *j*, *k*, and *l* in **Figure 3**a. The nucleation energy barriers near these positions are perceptibly lowered. Once an opposite voltage of –4 V is applied using the PFM tip-scanning across the whole film area, the domains near these sites grow first, as shown in Figure 3b. These observations confirm inhomogeneous domain nucleation near the defect sites, in agreement with the previous studies.[12–14,24,25]

Apart from the α dependence on the film area, α also varies with T according to $v \propto \exp(-\Delta U/k_B T)$, as shown in **Figure 4**a–c for PZT1, PZT2, and PZT3, where the $\ln J_{sw}$–E_c^{-1} dependence is the average of the plots across region (b). Similar to the converged plots across the film area in Figure 2d–f, all of the plots at different T values also cross at the point (J_0, E_0) with $J_0 = 1.4 \times 10^8$ A cm^{-2}, in agreement with the previous measurements in 140-nm-thick PZT films. Therefore, the ultimate domain switching time of $\tau_0 = 0.47$ ps is independent of both the film thickness and area, which is probably limited by the E(TO) soft-mode frequency (lowest energy long-wavelength optical phonon). Raman spectra show the independence of the low-frequency soft modes of E(1TO) and A_1(TO) in PZT3 on T ranging between 77 and 300 K (Supporting Information Figure S3), so that the $\ln J_{sw}$–E_c^{-1} plots can converge at (J_0, E_0) in the theory. This thickness independence rules out the contribution of the domain forward growth time across the film thickness and provides rigorous evidence of the nucleation-rate-controlled domain switching mechanism.

However, the saturation switching field of E_0 in region (b) does depend slightly on the film thickness, d, and decreases from 0.28 MV cm^{-1} in PZT1 to 0.21 MV cm^{-1} in PZT3, as shown in Figure 4a–c. This E_0 variation with d may arise from the interfacial

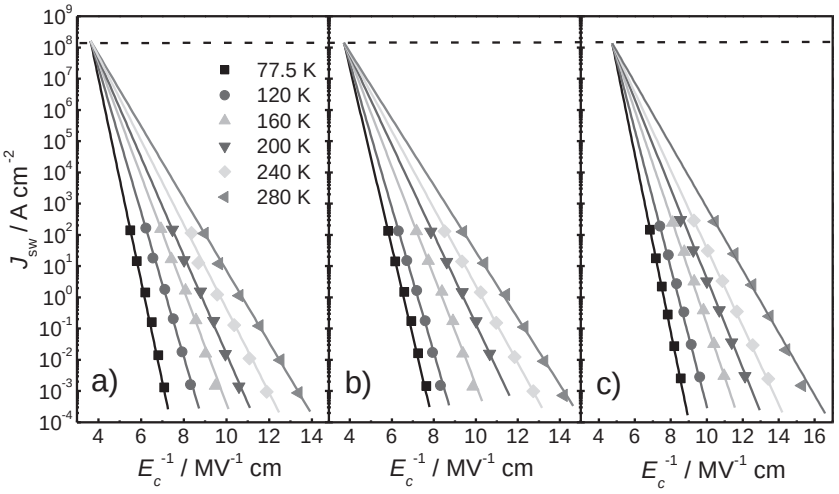

Figure 4. Dependence of the domain switching current density on the inverse of the coercive field at different temperatures for PZT with thicknesses of a) 0.5 μm, b) 1 μm, and c) 2 μm. The solid lines that converge at the point (J_0,E_0) are the best fits of the data according to Equation (1).

layer effect of finite-screening length of the top and bottom electrodes and the near-electrode non-ferroelectric passive layers.[29–31] The interfacial layers are an inherent feature of many dielectric/metal interfaces, but can be engineered out in specific cases where there is particularly weak interface bonding.[32] **Figure 5** shows the thickness dependence of the coercive voltages at different J_{sw} values at 240 K. Although the dependence is linear, all of the plots cross the d axis with a nonzero intercept of d_i = –82 nm. Theoretically, $|d_i|$ is the equivalent PZT thickness of the interfacial layers under an external voltage, which is T independent, as shown in the inset of Figure 5. Therefore, the total film thickness under V can be regarded as $d+|d_i|$ for consideration of the interfacial-layer effect, and E_0 becomes 0.24 MV cm^{-1}, 0.25 MV cm,$^{-1}$ and 0.20 MV cm^{-1} for the three films after this interfacial-layer correction, comparable to 0.20 MV cm^{-1} in a 140-nm-thick PZT film and 0.27 MV cm^{-1} in ref. [27] within experimental uncertainty limits.[9] Therefore, the inferred 82 nm of the equivalent interfacial layer thickness is plausible.

Figure 6 shows the temperature dependence of the reciprocal activation field before (closed symbols) and after (open symbols) the interfacial-layer correction for PZT1, PZT2, and PZT3 across region (b). The plots differing with the film thickness before the thickness correction are made but coincide after inclusion of the interfacial layers. From the Miller–Weinreich nucleation model,[22] the inverse of the activation field in the Merz equation is:

$$\frac{1}{\alpha} = \frac{3\sqrt{3}k_B\varepsilon^{1/2}}{16a^{3/2}\sigma_w^{3/2}\left(\ln\frac{4\sigma_w}{3aP_sE_c}\right)^{1/2}}T \quad (5)$$

where a is the lattice constant, ε is the dielectric permittivity, k_B is the Boltzmann constant, and σ_w is the wall energy. According to this model, the α^{-1}–T plot should be linear and pass through the origin. From our experimental observations, the plots in Figure 6 are indeed linear, as confirmed from solid-line fitting of the data, but miss the origin with a finite intercept on the positive α^{-1} axis. To overcome this difficulty, one should consider the contribution of the zero-point energy to the thermal energy of domain nucleation by using the Einstein energy.[9,33,34] With the assumption of $a \approx 4.0$ Å, $\varepsilon \approx 458$ (Supporting Information Figure S4) and $P_s \approx 40$ μC cm^{-2}, the 180° domain-wall energy along the low-index (100) lattice plane in PZT thick films was estimated to be 26 mJ cm^{-2} at E_c = 150 kV cm^{-1}, which is far smaller than the theoretical wall energy of 168 mJ m^{-2} found from atomistic calculations of $Pb(Zr_{0.5}Ti_{0.5})O_3$ with

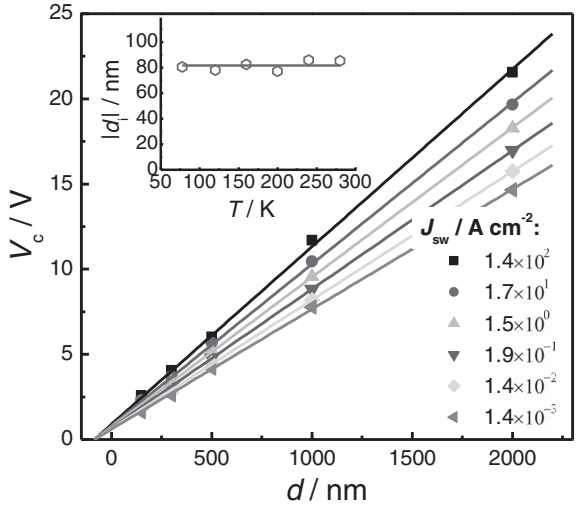

Figure 5. Film thickness dependence of the coercive voltage at different domain switching current densities at 240 K. The solid lines that converge at the d axis are the linear fits of the data. The inset shows the temperature independence of the equivalent interfacial layer thickness fitted by a solid line.

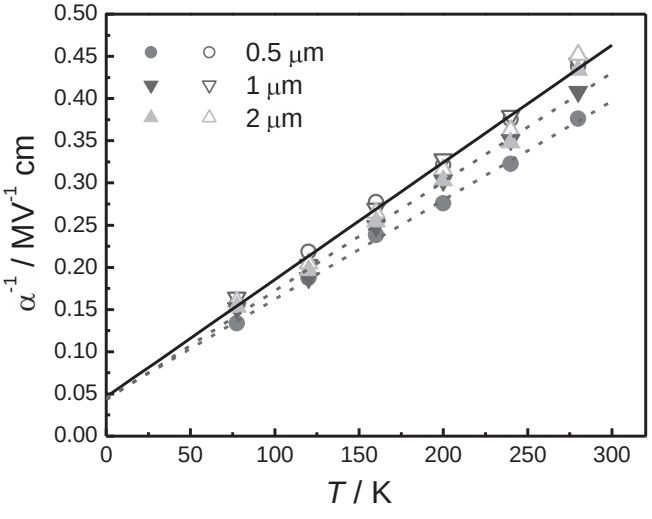

Figure 6. Temperature dependence of the reverse of the activation field for region (b) with different film thicknesses. The closed and open symbols allow comparison of the plots before and after the interfacial-layer correction, where the dashed and solid lines are linear fits of the data according to Equation (5).

Zr centered 180° walls, possibly due to the oversimplified Miller–Weinreich model without consideration of the diffuseness of the polarization change across the wall.[23,35]

3. Conclusions

From the time discretization of the domain switching current transient into individual domain switching regions across the film area in the order of $0 < V_c(t_1) < V_c(t_2) < V_c(t_3) <\ldots$ with $t_1< t_2 < t_3<\ldots$, it is possible to explore the switching kinetics of each domain with a different nucleation energy near a preferred defect site at various applied voltages and temperatures. Although the activation field varies with the film area as well as temperature, the ultimate domain switching current density at a saturation field is constant after inclusion of the interfacial layers. This thickness independence of the subpicosecond domain switching process strongly supports nucleation rate-limited domain switching for film thicknesses of 0.14–2 μm. This finding facilitates functional thick-film applications in ultrafast electronic, optoelectronic, electrochemical, and electromechanical devices. All of the $\ln J_{sw}$–E_c^{-1} plots at different temperatures and regions across the inhomogeneous film area converge at the point (J_0,E_0), which shows the unimportance of diverging thermal nucleation energies near various imperfection sites on the ultimate domain nucleation time and strength.

4. Experimental Section

Both PZT thin and thick films (received from Inostek Inc., South Korea) were prepared by sol-gel spin coating on $Pt/Ti/SiO_2/Si$ substrates. The precursors of lead acetate trihydrate, zirconium propoxide, and titanium butoxide-based solutions were prepared and spin-coated onto a substrate at 4000 rpm for 20 s. The deposited layer was initially heated to 450 °C for 10 min and then annealed at 650 °C for 2 min. The deposition procedure was repeated until a required thickness was reached, and all of the layers were finally annealed at 650 °C for 30 min. Pt top electrodes were sputtered on the films through a shadow mask with an electrode area of between 2.8×10^{-4} and 5.5×10^{-4} cm^2.

Function-step voltage pulses with rise times of 8 ns were supplied on PZT top electrodes by an Agilent 8114A pulse generator with an internal resistance of 50 Ω. The domain switching response after a presetting pulse was monitored using an LC WR 6200A oscilloscope. The samples were cooled with liquid nitrogen flowing through a cryogenic LakeShore probe station interfaced with a Model 332 temperature controller. Capacitance–voltage curves were collected using an Agilent E4980A Precision LCR meter with a voltage amplitude of 0.05 V at 100 kHz. The *P*–*E* hysteresis loops were recorded using a Radiant Materials Precision Analyzer with a triangular wave at 1 kHz. The film structure was analyzed using X-ray diffraction (Bruker X-ray Diffractometer D8) and scanning electron microscopy (XL30 FEG). PFM (Veeco MultiMode V) with a commercial Pt coated Si tip (NT-MDT) was carried out to study the local domain switching dynamics at room temperature with a tip force constant of 0.2 N m^{-1} and an AC amplitude of 1 V at 147 kHz. The low-temperature Raman study of the soft-mode frequencies was performed using a micro-Raman spectrometer (Jobin-Yvon LabRAM HR 800 UV) in a laser line of 488 nm.

Supporting Information

Supporting Information is available from the Wiley Online Library or from the author.

Acknowledgements

The authors thank Prof. Z. G. Hu for the Raman study. This work was supported financially by the National Natural Foundation of China (No. 61176121) and the Shanghai Key Program (No. 1052nm07600).

Received: November 23, 2011
Published online: February 21, 2012

[1] Y. Xia, P. Yang, Y. Sun, Y. Wu, B. Mayers, B. Gates, Y. Yin, F. Kim, H. Yan, *Adv. Mater.* **2003**, *15*, 353.
[2] H. Han, Y. Kim, M. Alexe, D. Hesse, W. Lee, *Adv. Mater.* **2011**, *23*, 4599.
[3] P. M. Rorvik, T. Grande, M.-A. Einarsrud, *Adv. Mater.* **2011**, *23*, 4007.
[4] S. H. Choy, X. P. Jiang, K. W. Kwok, H. L. W. Chan, *Ceram. Int.* **2010**, *36*, 2345.
[5] S. T. Lau, H. F. Ji, X. Li, W. Ren, Q. Zhou, K. K. Shung, *IEEE Trans. Ultrason. Ferroelectr. Freq. Control* **2011**, *58*, 249.
[6] J. F. Scott, C. A. P. de Araujo, *Science* **1989**, *246*, 1400.
[7] D. S. Rana, I. Kawayama, K. Mavani, K. Takahashi, H. Murakami, M. Tonouchi, *Adv. Mater.* **2009**, *21*, 2881.
[8] J. Li, B. Nagaraj, H. Liang, W. Cao, C. H. Lee, R. Ramesh, *Appl. Phys. Lett.* **2004**, *84*, 1174.
[9] A. Q. Jiang, H. J. Lee, C. S. Hwang, J. F. Scott, *Adv. Funct. Mater.* **2012**, *22*, 192.
[10] J. F. Meng, R. S. Katiyar, G. T. Zou, X. H. Wang, *Phys. Status Solidi A* **1997**, *164*, 851.
[11] M. R. Joya, P. S. Pizani, *Appl. Phys. Lett.* **2010**, *97*, 031903.
[12] S. Jesse, B. J. Rodriguez, S. Choudhury, A. P. Baddorf, I. Vrejoiu, D. Hesse, M. Alexe, E. A. Eliseev, A. N. Morozovska, J. Zhang, L.Q. Chen, S. V. Kalinin, *Nat. Mater.* **2008**, *7*, 209.
[13] S. Hong, N. Setter, *Appl. Phys. Lett.* **2002**, *81*, 3437.
[14] S. Hong, B. Ecabart, E. L. Colla, N. Setter, *Appl. Phys. Lett.* **2004**, *84*, 2382.
[15] P. Paruch, T. Giamarchi, J. M. Triscone, *Phys. Rev. Lett.* **2005**, *94*, 197601.
[16] X. F. Du, I. W. Chen, *J. Appl. Phys.* **1998**, *83*, 7789.
[17] X. F. Du, I. W. Chen, *Appl. Phys. Lett.* **1998**, *72*, 1923.
[18] A. K. Tagantsev, I. Stolichnov, N. Setter, J. S. Cross, M. Tsukada, *Phys. Rev. B* **2002**, *66*, 214109.
[19] W. J. Merz, *Phys. Rev.* **1954**, *95*, 690.
[20] R. C. Miller, A. Savage, *Phys. Rev.* **1959**, *115*, 1176.
[21] R. Landauer, *J. Appl. Phys.* **1957**, *28*, 227.
[22] R. C. Miller, G. Weinreich, *Phys. Rev.* **1960**, *117*, 1460.
[23] Y.-H. Shin, I. Grinberg, I.-W. Chen, A. M. Rappe, *Nature* **2007**, *449*, 881.
[24] T. Tybell, P. Paruch, T. Giamarchi, J.-M. Triscone, *Phys. Rev. Lett.* **2002**, *89*, 097601.
[25] A. Gruverman, B. J. Rodriguez, C. Dehoff, J. D. Waldrep, A. I. Kingon, R. J. Nemanich, J. S. Cross, *Appl. Phys. Lett.* **2005**, *87*, 082902.
[26] A. Gruverman, D. Wu, J. F. Scott, *Phys. Rev. Lett.* **2008**, *100*, 097601.
[27] J. F. Scott, L. Kammerdiner, M. Parris, S. Traynor, V. Ottenbacher, A. Shawabkeh, W. F. Oliver, *J. Appl. Phys.* **1988**, *64*, 787.
[28] A. Q. Jiang, Y. Y. Lin, T. A. Tang, *J. Appl. Phys.* **2007**, *101*, 104105.
[29] J. Junquera, P. Ghosez, *Nature* **2003**, *422*, 506.
[30] S. P. Alpay, I. B. Misirlioglu, V. Nagarajan, R. Ramesh, *Appl. Phys. Lett.* **2004**, *85*, 2044.
[31] L. J. Sinnamon, R. M. Bowman, J. M. Gregg, *Appl. Phys. Lett.* **2001**, *78*, 1724.
[32] L.-W. Chang, M. Alexe, J. F. Scott, J. M. Gregg, *Adv. Mater.* **2009**, *21*, 4911.
[33] C. L. Wang, J. C. Li, M. L. Zhao, J. L. Zhang, W. L. Zhong, C. Arago, M. I. Marques, J. A. Gonzalo, *Physica A* **2008**, *387*, 115.
[34] W. Kleemann, J. Dec, B. Westwánski, *Phys. Rev. B* **1998**, *58*, 8985.
[35] S. P. Beckman, X. Wang, K. M. Rabe, D. Vanderbilt, *Phys. Rev. B* **2009**, *79*, 144124.